Geopotential Field Anomaly Continuation with Multi-Altitude Observations

Jeong Woo Kim[1], Hyung Rae Kim[2], Ralph von Frese[3], Patrick Taylor[4], Elena Rangelova[1]

[1] Dept. of Geomatics Engineering, The University of Calgary, Calgary, AB T2N1N4, CANADA
[2] Dept. of Geoenvironmental Sciences, Kongju National University, Kongju, 314-701, KOREA
[3] School of Earth Sciences, The Ohio State University, Columbus, OH 43210, USA
[4] Goddard Space Flight Center, National Aeronautics and Space Administration, Greenbelt, MD 20771, USA

ABSTRACT

Conventional gravity and magnetic anomaly continuation invokes the standard Poisson boundary condition of a zero anomaly at an infinite vertical distance from the observation surface. This simple continuation is limited, however, where multiple altitude slices of the anomaly field have been observed. Increasingly, areas are becoming available constrained by multiple boundary conditions from surface, airborne, and satellite surveys. This paper describes the implementation of continuation with multi-altitude boundary conditions in Cartesian and spherical coordinates and investigates the advantages and limitations of these applications. Continuations by EPS (Equivalent Point Source) inversion and the FT (Fourier Transform), as well as by SCHA (Spherical Cap Harmonic Analysis) are considered. These methods were selected because they are especially well suited for analyzing multi-altitude data over finite patches of the earth such as covered by the ADMAP database. In general, continuations constrained by multi-altitude data surfaces are invariably superior to those constrained by a single altitude data surface due to anomaly measurement errors and the non-uniqueness of continuation.

Key words: Anomaly continuation, equivalent point source inversion, Fourier transform, spherical cap harmonic analysis

I. INTRODUCTION

In practice, no gravity or magnetic observation can be made with infinite accuracy. Thus, the further apart the truncated observations are from each other, the more biased they will be to different spatial attributes of the sources. This result makes it extremely problematic to relate, for example, truncated satellite altitude anomaly observations over hundreds of kilometers to imperfectly measured observations at the earth's surface by simple downward continuation of the satellite data or upward continuation of the near-surface data (e.g., Schnetzer, 1985; Grauch, 1993; von Frese et al., 1999; 2005; Ravat et al., 2002; Kim et al., 2004; 2005). Measurement errors alone restrict the utility of spaceborne anomaly continuations typically to within approximately ±50 km of mission altitude (von Frese et al., 2005). The problematic attributes of downward continuation, in particular, require that analyses of spaceborne geopotential observations be conducted essentially at satellite altitudes, unless they are integrated into a model that is also constrained by lower altitude observations.

Measurement errors also result in uncertainties in the spectral properties of the anomaly observations that grow with increasing difference in the survey altitudes. **Figure 1**, for example, compares the spectral properties of North American crustal magnetic anomalies mapped by typical satellite surveys at 400 km (e.g., Magsat and CHAMP) and the Decade of North American Geology (DNAG) compilation of aeromagnetic survey data (Hildenbrand et al., 1996). The comparison reveals a significant spectral gap between the two data sets with wavelengths comparable in scale to the magnetic effects of major crustal features. Due to measurement errors and the fundamental non-uniqueness of potential field continuation, there ultimately is no substitute to actual surveying for recovering these intermediate wavelength anomalies. Here, the intermediate wavelength anomalies might be substantially recovered by additional surveying at 20 km altitude with U2 surveillance or other high-altitude aircraft (Hildenbrand et al., 1996).

Global spherical harmonic models of the Earth's gravity (*e.g.*, Lemoine et al., 1998) and magnetic (Maus et al., 2009) fields are becoming increasingly available which are constrained by both satellite altitude and near-surface (i.e., terrestrial, marine and airborne) measurements. However, in contrast to the nearly global coverage that the satellite surveys provide, the coverage from near-surface surveys is far from global. Thus, when implementing near-surface predictions

60 from these models, particular care must be taken to verify that the predictions are constrained by
61 actual survey data.

62 Most geological gravity and magnetic anomaly studies tend to invoke local patches of
63 coverage and complementary subsurface geological and geophysical constraints that are difficult
64 to accommodate at the global scale of spherical harmonic modeling (*e.g.*, von Frese and Kim,
65 2003). Alternate approaches that are well suited for local applications in Cartesian and spherical
66 coordinates include equivalent point source (EPS) inversion, the Fourier transform (FT) in
67 Cartesian coordinates, and spherical cap harmonic analysis (SCHA) in spherical coordinates.
68 These procedures are all applicable to gravity and magnetic studies of the Antarctic lithosphere
69 south of 60°S. The sections below describe their uses for continuing multi-altitude data and
70 consider the relative advantages and limitations of these applications.
71

72 **II. EQUIVALENT POINT SOURCE (EPS) CONTINUATION**

73 In this section, EPS inversion is investigated for modeling anomaly continuations based on
74 single- and dual-altitude boundary conditions and using satellite crustal anomalies to fill in the
75 gaps in the near-surface survey coverage of the ADMAP database. EPS inversion has a long
76 history of estimating interpolations, continuations, and other derivative and integral components
77 of anomaly observations (e.g., Dampney, 1969; Ku, 1977; Mayhew, 1982; von Frese et al., 1981;
78 1998; Asgharzadeh et al., 2007; 2008).

79 The EPS effect is the fundamental integrand for all forward modeling integrals in gravity and
80 magnetic analysis (e.g., Blakely, 1995). For typical crustal ADMAP applications, it is
81 convenient to express the gravity point pole and magnetic point dipole effects in terms of the
82 spherical prism. More specifically, the gravity effect of the crustal prism in spherical (r, θ, φ)
83 coordinates with uniform density (= mass/unit volume) contrast $\Delta\sigma$ (e.g., von Frese et al., 1981;
84 Asgharzadeh et al., 2007) is

85 $$\Delta g(r,\theta,\varphi) \approx \Delta\varphi'_l \sum_{l=1}^{nl}\{\Delta\theta'_j \sum_{j=1}^{nj}(\Delta r'_i \sum_{i=1}^{ni}[-G\frac{\partial}{\partial R}(\frac{1}{R})\frac{\partial R}{\partial r}\Delta\sigma]A_i r_i^{\,2})A_j \sin\theta_j\}A_l \ , \qquad (1)$$

where G is the universal gravitational constant, R is the displacement between the source and observation points with respectively primed and unprimed coordinates, and (A_i, A_j, A_l) are the Gaussian-Legendre quadrature coefficients for the (nl×nj×ni) point sources used to approximate the prism's volume (e.g., Stroud and Secrest, 1966). In addition,

$$\Delta\varphi'_l = [(\varphi'_{la} - \varphi'_{lb})/2], \Delta\theta'_j = [(\theta'_{ja} - \theta'_{jb})/2], \Delta r'_i = [(r'_{ia} - r'_{ib})/2] \ , \qquad (2)$$

where (φ'_{la}, φ'_{lb}), (θ'_{ja}, θ'_{jb}), and (r'_{ia}, r'_{ib}) are the lower (a) and upper (b) boundaries of the prism in the l-th coordinate of longitude (φ), the j-th coordinate of co-latitude (θ), and i-th radial coordinate (r). For completeness, note that Ku (1977) gives the equivalent Gauss-Legendre quadrature (GLQ) gravity effect of the prism in Cartesian coordinates.

The total magnetic effect (ΔT) of the crustal prism, on the other hand, with uniform magnetization (= dipole moment/unit volume) contrast Δm in spherical coordinates (e.g., von Frese et al., 1981; 1998; Asgharzadeh et al., 2008) is

$$\Delta T(r,\theta,\varphi) \approx \Delta\varphi'_l \sum_{l=1}^{nl}\{\Delta\theta'_j \sum_{j=1}^{nj}(\Delta r'_i \sum_{i=1}^{ni}[\vec{u}\bullet\vec{\nabla}\{\vec{u}'\bullet\vec{\nabla}'(\frac{1}{R})\}\Delta m]A_i r_i'^2)A_j \sin\theta_j\}A_l \ , \qquad (3)$$

where the unit vectors $\vec{u}'$ in source coordinates (r', θ' φ') and $\vec{u}$ in observation coordinates (r, θ, φ) are dotted into the source and observation coordinate gradient operators $\vec{\nabla}'$ and $\vec{\nabla}$, respectively. The magnetization contrast Δm represents the integrated effect of remanent and induced components, where the latter is the prism's volume magnetic susceptibility times the intensity of the applied magnetic field at the source point. Again for completeness, note that Ku (1977) gives the equivalent magnetic effect of the prism by GLQ integration in Cartesian coordinates.

Now, continuation, like any potential field analysis, can be generalized in matrix notation by

$$\mathbf{AX} = \mathbf{B}, \qquad (4)$$

where **B** is the (n×1) column matrix containing the n-anomaly observations, and **AX** is the forward model involving the (n × m) known coefficients of the design matrix **A** and the (m×1)

column matrix containing the m-unknown coefficients of the solution matrix **X**. The objective for continuation is to find the coefficients of **X** such that **AX** closely models **B** whereupon **AX** may be used evaluate the attributes of **B** at other coordinates. Most typically, the least squares solution is found by

$$\mathbf{X} = [\mathbf{A}^T\mathbf{A}]^{-1}\mathbf{A}^T\mathbf{B} \tag{5}$$

so that the sum of the squared residuals between the observations and the forward model's predictions is minimum (e.g., von Frese et al., 1988).

Eq. 2 and **Eq. 3** provide the forward models for relating respective gravity and magnetic anomalies to prism models that can be used for anomaly continuation. In particular, by specifying the geometric attributes of the prism model, the inversion (**Eq. 4**) can be set up to solve for the respective density and magnetization contrasts (**Eq. 5**) so that the modeled predictions (**AX**) match the observations (**B**) in a least squares sense. To obtain the coefficients of the design matrix **A**, the model is initialized by simply running it with the physical property (i.e., $\Delta\sigma$ or Δm) set to unity.

In practice, however, errors in computing the **A**-coefficients due to the computer's limited working precision and other uncertainties in the forward modeling may yield an unstable solution **X** with large and erratic values that are useless for predicting anything other than the original observations in **B**. To obtain a more stable and better performing solution, the system in **Eq. 3** is commonly evaluated for the damped least squares solution

$$\mathbf{X} = [\mathbf{A}^T\mathbf{A} + (\mathrm{EV}) \times \mathbf{I}]^{-1}\mathbf{A}^T\mathbf{B}\,, \tag{5}$$

where **I** is the identity matrix, and the scalar EV is variously called the damping factor, Marquardt parameter, or error variance (e.g., von Frese et al., 1988). The damped least squares approach requires choosing a value of EV that is just large enough to stabilize the solution for meaningful objective predictions (e.g., anomaly continuation, interpolation, etc.), yet small enough that the initial predictions provide an acceptable match to the observations **B**. For any set of observations and forward model, an essentially optimal value of EV can be selected from trade-off diagrams that contrast these two sets of model predictions for varying EV-values (e.g., von Frese et al., 1988).

Adapting the above results for anomaly continuation constrained by one or more boundary conditions is straightforward. Relating both airborne and satellite anomaly observations to a crustal prism model, for example, involves constructing the design matrix $\mathbf{A} = [\mathbf{A}_{airborne}\ \mathbf{A}_{satellite}]^T$ for the observation vector $\mathbf{B} = [\mathbf{B}_{airborne}\ \mathbf{B}_{satellite}]^T$, where the submatrices $\mathbf{A}_{airborne}$ and $\mathbf{A}_{satellite}$ reflect the geometric relationships between the crustal prism source coordinates and the coordinates of the airborne and satellite observations in the respective $\mathbf{B}_{airborne}$ and $\mathbf{B}_{satellite}$ subvectors.

To test the performance of single- *versus* multi-altitude boundary conditions in anomaly continuation, **Eq. 2** and **Eq. 3** were used to model the respective gravity and magnetic effects of the five crustal prisms (**Figure 2**) outlined in top left anomaly maps of **Figure 3** and **Figure 4**, respectively. The prisms were modeled for density contrasts ranging between -1.2 g/cm^3 and 1.8 g/cm^3, and cgs-magnetic susceptibility of contrasts of 0.0061468 and -0.028831 relative to the surrounding crustal rocks. All prisms were 25 km thick with tops at 5 km below sea level and located in Balkan region between 34° - 43° N and 21°- 30° W. the panel A of maps in **Figure 3** shows the modeled gravity effects to the nearest mGal over a 35×35 grid spanning the study area at altitudes of 5 km (top), 10 km, 100 km, 200 km, 400 km, and 600 km (bottom). Panel A of **Figure 4** gives the complementary differentially reduced-to-pole (DRTP) magnetic effects to the nearest nT (e.g., von Frese et al., 1981). The DRTP effects were obtained from **Eq. 3** assuming vertical inclination of the applied field at all source and observation points with the field intensities at all source points taken from the World Magnetic Model (WMM) 2005 (NOAA, 2005).

The continuation analysis focused on relating the simulated airborne and satellite altitude effects at 10 km and 400 km above sea level, respectively, to 50×50 arrays of crustal point masses and magnetic dipoles at depths of 40 km and 20 km, respectively, below sea level. These EPS inversions used the simpler forward model given by the integrands within the square brackets of **Eq. 2** and **Eq. 3** to obtain the relevant point mass (= $\Delta\sigma$ × unit volume) and dipole moment (= Δm×unit volume) solutions, respectively. In the two figures, the **B-panels** show the predictions from the EPS solutions constrained by the anomalies modeled at both 10 km and 400 km above sea level, whereas the **C-** and **D-panels** give the continuations derived only from the single-surface effects at the respective 10 km and 400 km altitudes. Comparison of the dual-

surface continuations in the **B-panels** with the equivalent single-surface estimates in the **C-** and **D-panels** amply demonstrates the advantages of multi-altitude constrained continuation models especially for downward continuation.

The comparisons at 5 km, and 10 km through 600 km altitudes at 10 km intervals are detailed further in **Figure 5**. The respective left and right panels demonstrate the performances of the gravity and magnetic continuations in terms of their correlation coefficients and root-mean-squared (RMS) differences with the effects of the five prisms. These results, of course, like those from any potential field analysis, are not unique. However, they clearly demonstrate the limitations of downward continuing satellite-only potential field observations. They also suggest that the multi-altitude magnetic continuations could be improved by incorporating additional data from around 60 km to 80 km altitudes.

EPS models constrained by satellite and near-surface magnetic data are effective for filling in regional gaps in the near-surface survey coverage in the ADMAP compilation, which are particularly extensive in East Antarctica. The first compilation used satellite magnetic observations from the 400-km altitude, 6-month Magsat mission (Golynsky et al., 2001). However, these satellite data were collected during austral summer and fall periods, and thus maximally corrupted by external magnetic field variations. The Ørsted and CHAMP missions obtained much cleaner Antarctic satellite magnetic observations from several austral winters at altitudes of about 600 and 400 km, respectively, with measurement accuracies exceeding Magsat's by roughly an order of magnitude. The initial Magsat-based predictions in the ADMAP compilation have been replaced by Ørsted- and CHAMP-based gap predictions (von Frese et al., 2008).

To obtain effective estimates of near-surface anomalies in the coverage gap, the inversion of the satellite data was optimized to match the near-surface anomaly observations around the gap's perimeter (Kim et al., 2004; 2007). **Figure 6** illustrates the relative utility of this approach for a simulated regional gap in ADMAP's near-surface survey coverage of the West Antarctic Peninsula and surrounding marine areas (Kim et al., 2004). **Map A** shows the original ADMAP 10-km grid at 5-km above sea level of marine and airborne survey data for the well covered region. Due to the mission altitudes, the satellite data are mostly sensitive to the 400-km and

larger wavelength components of the near-surface data in **Map B**. The low-pass filtered data were related to a crustal prism model with negligible error that was evaluated at 400 km altitude with an accuracy of 3 nT in **Map C** to simulate the effects of Magsat measurement errors. The crustal prism model was also evaluated to a 0.3 nT accuracy at altitudes of 400 km in **Map E** and 700 km in **Map G** to simulate the respective effects of CHAMP and Ørsted satellite observation errors.

The simulated Magsat, CHAMP, and Ørsted data were combined with the near-surface data around the white-outlined periphery of the simulated gap in **Map B** and related to crustal prism models by least squares inversion. The resultant prism models were then evaluated for the respective Magsat-, CHAMP-, and Ørsted-based gap predictions shown in **Maps D**, **F**, and **H**. **Table 1** compares the gap predictions against the original gap values from **Map B** in terms of the RMS differences, correlation coefficients (CC) and noise levels from the noise (N)-to-(S) signal ratio approximation (Foster and Guinzy, 1967) given by

$$\frac{N}{S} \approx \sqrt{\frac{1}{|CC|} - 1}\,. \tag{6}$$

The comparison also includes gap predictions from the application of minimum curvature (MC) to the near-surface survey data. In general, the simulated results suggest that the use of the Ørsted and CHAMP data improves the gap estimates by nearly 75% relative to the Magsat-based predictions.

An opportunity to test the multi-altitude gap prediction method resulted when a new aeromagnetic survey was obtained in the regional gap located east of Coats Land and the Shackleton Range as shown in **Map A** of **Figure 7** (Kim et al., 2007). **Map B** gives the regional 200 km and longer wavelength components of the new survey data that are much more consistent with the CHAMP- and Ørsted-based gap predictions in **Map C** than with the minimum curvature estimates in **Map D** and the near-surface predictions of the spherical harmonic geomagnetic field model MF4 (Maus and Rother, 2005) in **Map E**.

Of course, as for any inversion, the results of continuation are not unique. Thus, they do not obviate the need for anomaly mapping in regions lacking measurements to better define the geologic implications in existing anomaly observations.

III. FOURIER TRANSFORM (FT) CONTINUATION

Gravity and magnetic anomalies are mapped at elevations accessible by borehole, tunnel, ground and ice surface, ocean and lake bottom, submarine, ship, airplane, balloon, space shuttle tether, and satellite surveys. Where the horizontal dimensions of the survey are several hundred kilometers or less, the data are commonly gridded at constant elevation and horizontal intervals measured in linear units of length for analysis. In this case where the anomaly data are registered to a Cartesian grid, effective anomaly continuation can be done most elegantly and efficiently using the Fourier transform as the forward model of the inversion (e.g., Blakely, 1995).

The free-space behavior of gravity and magnetic anomalies S is governed by Laplace's equation

$$\left(\frac{\partial^2}{\partial x^2}+\frac{\partial^2}{\partial y^2}+\frac{\partial^2}{\partial z^2}\right)S=0 \tag{7}$$

so that the vertical z-dimensional properties of the anomalies may be assessed from their mapped x- and/or y-dimensional attributes. In particular, for gridded $S(x, y)$ with the gridded Fourier transform $\overline{S}(l,k)$ in wavenumbers l and k, taking the Fourier transform of **Eq. 7** gives

$$\frac{\partial^2\overline{S}}{\partial z^2}=(2\pi)^2(f_l^2+f_k^2)\overline{S}\ , \tag{8}$$

where ($f_l = l/M$) and ($f_k = k/N$) are the linear frequencies for the number of anomaly values M and N in the x- and y-directions, respectively. **Eq. 8** is a second order differential equation with constant coefficients that has the general solution

$$\overline{S}(z)=A\times e^{+z\sqrt{a}}+B\times e^{-z\sqrt{a}}, \tag{9}$$

where

$$a=4\pi^2(f_l^2+f_k^2). \tag{10}$$

Boundary conditions are commonly invoked to specify the form of the solution in **Eq. 9** that is appropriate for application. By the classical Poisson boundary condition, acceptable solutions

252 are those that approach zero as the elevation z becomes infinite. Thus, for upward continuation
253 where $z > 0$, the boundary condition requires $A = 0$ so that the solution becomes

254 $$\bar{S}(z)_{upcon} = B \times e^{-z\sqrt{a}}. \quad (11)$$

255 Referencing the grid to $z = 0$ shows that $B = \bar{S}(0) \equiv \bar{S}$ so that the upward continuation of
256 the anomaly grid to any positive $z > 0$ is

257 $$\bar{S}(z)_{upcon} = \bar{S} \times e^{-z\sqrt{a}}. \quad (12)$$

258 Similarly, for downward continuation where $z < 0$, the boundary condition requires $B = 0$ so
259 that the solution is
260

261 $$\bar{S}(z)_{dwcon} = A \times e^{+z\sqrt{a}}. \quad (13)$$

262 Again, taking the elevation of the grid as relative zero shows that $A = \bar{S}(0) \equiv \bar{S}$ so that the
263 downward continuation of the anomaly grid to negative $z < 0$ is

264 $$\bar{S}(z)_{dwcon} = \bar{S} \times e^{+z\sqrt{a}}. \quad (14)$$

265 Inversely transforming **Eq. 12** and **Eq. 14** is the conventional approach for upward and
266 downward continuing a single anomaly grid through positive and negative elevations about its
267 elevation (e.g., Pawlowski, 1995; Fedi and Florio, 2002; Cooper, 2004). The singular uses of the
268 A and B coefficients in **Eq. 9** define the two end member solutions for downward and upward
269 continuation, respectively. However, multiple altitude anomaly grids are becoming increasingly
270 available where both coefficients may be applied to evaluate the anomaly values at the
271 intermediate altitudes between the grids.

272 Specifically, let the lower altitude anomaly grid be referenced to relative zero and the higher
273 altitude grid be referenced to an elevation H where the Fourier transforms of *S(0)* and *S(H)* are
274 $\bar{S}(0)$ and $\bar{S}(H)$, respectively. Both transforms may be related through **Eq. 9** to common A and
275 B coefficients given by

276

277 $$A = \frac{\bar{S}(0)e^{-z\sqrt{a}} - \bar{S}(H)}{e^{-z\sqrt{a}}} \quad \text{and} \quad B = \frac{\bar{S}(H) - \bar{S}(0)e^{+H\sqrt{a}}}{e^{-z\sqrt{a}}} \quad (13)$$

278

so that the continued field at an intermediate z-altitude for all $0 \le z \le H$ is

$$\bar{S}(z) = \frac{1}{t}\left[\bar{S}(0)e^{-H\sqrt{a}}e^{+z\sqrt{a}} - \bar{S}(H)e^{+z\sqrt{a}} + \bar{S}(H)e^{-z\sqrt{a}} - \bar{S}(0)e^{+H\sqrt{a}}e^{-z\sqrt{a}}\right]$$

$$= \frac{1}{t}\left[\bar{S}(0)\left(e^{+(z-H)\sqrt{a}} - e^{-(z-H)\sqrt{a}}\right) + \bar{S}(H)\left(e^{-z\sqrt{a}} - e^{+z\sqrt{a}}\right)\right] \qquad (14)$$

$$= \frac{1}{t}\begin{bmatrix} e^{+(z-H)\sqrt{a}} - e^{-(z-H)\sqrt{a}} \\ e^{-z\sqrt{a}} - e^{+z\sqrt{a}} \end{bmatrix}^{T}\begin{bmatrix} \bar{S}(0) \\ \bar{S}(H) \end{bmatrix},$$

with

$$t = e^{-H\sqrt{a}} - e^{+H\sqrt{a}}. \qquad (15)$$

Figure 8 illustrates the use of the dual Fourier transforms for two altitude slices of the noise-free gravity effects for a simple model of two prisms. The gravity effects of the prisms were calculated in Cartesian coordinates at relative 0 km (**Map A**) and at 16 km (**Map B**) and 20 km (**Map C**) above the relative 0-km effects. **Map D** shows the dual altitude continuation estimates at 16 km and **Map E** gives the difference between **Map B** and **Map D**. **Map F** is the conventional downward continuation of **Map C** at 16 km, whereas **Map G** is the 16-km upward continuation of **Map A** with **Map H** and **Map I** giving the related differences from the modeled effects in **Map B**. The dual and single surface continuations are largely consistent, although the dual surface estimates in **Map D** are clearly superior to the 4-km downward and 16-km upward continued single surface estimates in **Maps F and G**.

The general consistency of the single- and dual-surface continuations in **Figure 8** is mostly due to the source effects being minimally distorted in the two anomaly grids. This level of source signal fidelity is not likely to occur in practice where, for example, in the lower altitude grid the effects of near-surface sources mask within working precision elements of the more regional source effects that in the higher altitude grid are preferentially expressed at the expense of the shorter wavelength near-surface source effects. Measurement and anomaly reduction errors also will substantively affect the fidelity of gridded source signals at the different altitudes.

As an example, **Figure 9** considers the altitude variations of the reduced-to-pole magnetic anomalies over the southern Greenland area constrained by airborne (Verhoef et al., 1996) and CHAMP satellite (Maus et al., 2002) measurements. The magnetic data were Fourier transformed assuming the flat-earth approximation given the approximate 1,600 km by 1,600 km area of the study (Strang van Hees, 1990). The single surface transform was used to upward continue the airborne data to 20 km in **Map A**, 50 km in **Map B**, 250 km in **Map C**, 300 km in **Map D**, and 350 km in **Map E**. However, the CHAMP data at 350 km in **Map F** show a considerably stronger effect over Iceland than is apparent in the upward continued airborne data of **Map E**. Indeed, the dual surface FT continuations at 300 km in **Map G**, 250 km in **Map H**, and 50 km in **Map I** suggest that this disparity persists at altitudes of 250 km and higher. Clearly, the CHAMP data provide important additional constraints for developing a comprehensive crustal magnetic model of the study area.

IV. SPHERICAL CAP HARMONIC ANALYSIS (SCHA)

Spaceborne and lower altitude magnetic and gravity anomalies obviously provide different insights for resolving the crustal sources of the potential field anomalies. In particular, the lower altitude anomalies provide much more detail on the crustal sources than can be observed at satellite altitude. The satellite anomalies, on the other hand, typically yield better regional images of the sources than can be obtained from regional compilations of the lower altitude anomalies that have been mapped with disparate survey parameters. At regional scales of coverage such as represented by the ADMAP compilation for the Antarctic area south of 60^{o} S, the spherical cap harmonic synthesis of satellite and near-surface potential field observations is particularly useful and elegant model for crustal modeling. For example, it is analytically more useful than the simple grid for representing the ADMAP compilation because it can directly estimate magnetic anomalies and their gradient and tensor components anywhere on and above the Antarctic surface (e.g., von Frese et al., 2008).

Spherical cap harmonic analysis (SCHA) was developed by Haines (1985) for geomagnetic main and external magnetic field modeling at regional scales. It has also been extended to regional magnetic studies of the lithosphere (e.g., Haines and Newitt, 1986; De Santis et al., 1990; Kotzé, 2001; Thébault et al., 2006; Thébault and Gaya-Piqué, 2008; von Frese et al.,

2008), as well as gravity studies (e.g., Hwang and Chen, 2007; De Santis and Torta, 1997). This approach adapts the global spherical harmonic solution to a spherical cap solution for the magnetic potential

$$V(r,\theta,\varphi) = \sum_{n=0}^{N_{int}} \sum_{m=0}^{n} a\left(\frac{a}{r}\right)^{n+1} \left(g_n^{m,i} \cos m\varphi + h_n^{m,i} \sin m\varphi\right) P_n^m(\cos\theta) + \sum_{n=1}^{N_{ext}} \sum_{m=0}^{n} a\left(\frac{a}{r}\right)^{n} \left(g_n^{m,e} \cos m\lambda\varphi + h_n^{m,e} \sin m\varphi\right) P_n^m(\cos\theta), \quad (16)$$

where N_{int} and N_{ext} are the maximum indices for internal and external sources, respectively, P_n^m is a Legendre function of degree n and order m, and $g_n^{m,i}$, $h_n^{m,i}$, $g_n^{m,e}$, $h_n^{m,e}$ are the spherical cap Gauss coefficients. If the half-angle of the spherical cap is denoted by ϑ_0, the $n_k(m)$ for a given m are determined as the roots of

$$dP_n^m(\cos\theta_0)/d\theta = 0, k-m = \text{even}, \quad (17)$$

and additionally, where differentiability with respect to θ is required, of

$$dP_n^m(\cos\theta_0) = 0, k-m = \text{odd}. \quad (18)$$

Truncating the expansion in Equation (16) at $k = K$ sets the number of model coefficients at $(K+1)^2$. When applying SCHA, a global spherical harmonic potential is typically removed from the total potential to improve convergence as well as extrapolation beyond the spherical cap boundary (Haines, 1985). In general, the maximum degree of a spherical cap harmonic model, truncated at a certain number of model coefficients, is a function of the half-angle of the spherical cap that determines the minimum wavelength resolution that can be obtained (e.g., Kotzé, 2001). As a radial distance is also included in the formulation, data over a range of altitudes can be used to derive a model.

Two examples are presented in this study. The SCHA is a parametric method with the coefficients of the harmonic representation of the gravity and magnetic potential being model's parameters. This method has been proven to work with both gridded and irregularly distributed data, which in example are along track data. We used a variation of the SCHA, in which the spherical cap is mapped onto a hemisphere, thus ensuring the proper harmonic continuation of the gravity and magnetic field anomalies and to different altitudes between satellite and the Earth surface.

Figure 10 shows the use of SCHA to model the effects of the NE Asia gravity field developed by the Curtin University of Technology (CUT) in Western Australia (Kuhn and Featherstone, 2005). The gravity anomalies were synthesized on a 1^{o} x 1^{o} grid with the center of the spherical cap is 50^{o} N and 130^{o} E. In this example, the synthetic gravity anomaly data at the Earth's surface (c) and 20 km altitude (a) were jointly modeled by the SCHA with negligible error to obtain gravity anomalies at 10 km altitude (b) which show the compiled gravity anomalies at 10 km altitude with a resolution of 200 km half-wavelength. The model errors account for 10% of the gravity anomaly magnitude at most and can be further reduced by increasing the spectral resolution of the model. Table 2 shows the statistics of synthetic gravity data at 20, 10, and 0 km and correlation coefficients shown in **Figure 10**.

Another example modeling the radial geomagnetic field component at satellite (a), U2 (b) altitudes and the Earth surface (c) is given in **Figure 11**. Here, the satellite altitude (685 km) component for December 1999 was globally evaluated from the three-axis magnetometer measurements of the KOrea Multi Purpose Satellite-1 (KOMPSAT-1) that provided the satellite's attitude control (Kim et al., 2007) as shown **Figure 11** (a). These data were used to estimate the radial components by the SCHA at satellite (685 km), U2 (20 km) altitudes and at the Earth surface (0 km). Table 3 summarizes statistics and correlation coefficients of radial component of KOMPSAT-1 measurements estimated at satellite (685 km), U2 (20 km), and Earth surface (0 km) as shown in **Figure 11**. This example illustrates a further use of SCHA in developing improved regional core field models for extracting crustal components in the survey data.

392 The Antarctic Reference Model (ARM), for example, was developed for ADMAP
393 applications to best represent the spatial and temporal properties of the Antarctic core field as
394 recorded over the period 1960-2002 by an international network of 28 observatories and satellite
395 magnetic data from six missions (Gaya-Piqué et al., 2006). The SCHA predictions from ARM
396 have greater sensitivity for the Antarctic spatial and temporal variations of the core field than do
397 conventional global spherical harmonic geomagnetic field models like the IGRF-10 (IAGA,
398 2005).

399 Data from the Arctowski, Scott Base, Syowa, and Vostok geomagnetic observatory data
400 through 2003, for example, showed that the ARM estimates of the annual variations of the
401 Antarctic core field are roughly 31% and 22% better than the IGRF-10 and CM4 (Sabaka et al.,
402 2004) estimates, respectively. In addition, the core field predictions were checked at the Georg
403 von Neumayer observatory where data were obtained that had not been included in the original
404 ARM model. At this observatory, which was operated over the period 1983.5-1991.5 on the
405 coast of Dronning Maud Land (70.617° S, 351.633° E), the ARM estimates were found to be 76%
406 and 75% better than the respective IGRF-10 and CM4 estimates. Additionally, ARM estimated
407 the mean secular variation some 78% and 75% better than the respective IGRF-9 and CM4
408 models.
409

410 **V. CONCLUSIONS**

411 Low-earth-orbiting satellites are recording state-of-the-art magnetic and gravity field
412 observations of the earth at altitudes ranging over roughly 300-700 km. However, the
413 measurement errors and non-uniqueness of the continuation process severely limit estimating
414 these anomalies at the near-surface. Indeed, numerical anomaly simulations from satellite to
415 airborne altitudes suggest that effective downward continuations of the satellite data are
416 restricted to within approximately 50 km of the observation altitudes while upward continuations
417 can be effective over a somewhat larger altitude range. Given current anomaly error levels, the
418 multi-altitude inversion of satellite and near-surface anomalies is a particularly promising
419 approach for implementing satellite geomagnetic observations for crustal studies.

This study investigated multi-altitude implementations of equivalent point source (EPS) and spherical cap harmonic analysis (SCHA) modeling in spherical coordinates and the Fourier transform (FT) for continuation in Cartesian coordinates. These implementations revealed that the anomaly estimates at the intermediate altitudes from multi-altitude constrained models were invariably superior to the classical downward and upward continuations of a single slice of the anomaly field. In addition, near-surface downward continuations of satellite altitude observations or satellite altitude upward continuations of near-surface data can be severely problematic due to measurement and data reduction errors and the inherent non-uniqueness of any continuation. As a result, an observation's capacity to define a field's spatial behavior is restricted in practice to a relatively small region about the observation site beyond which mapping is required to confidently resolve the more distant spatial details of the field. In other words, there ultimately is no substitute for mapping to establish the value of an anomaly field at an unsurveyed location.

VI. ACKNOWLEDGMENTS

The National Science and Engineering Research Council (NSERC) of Canada supported this study under Discovery Grant #355477-2008. Elements of this research were performed at NASA's Goddard Space Flight Center in Greenbelt, MD while JWK held a US National Research Council Senior Research Associateship Award and HRK was Goddard Earth Sciences and Technology (GEST) fellow. The authors thank Drs. M.F. Asgharzadeh and J.S. Hwang for help with obtaining the simulation results.

VII. REFERENCES

Asgharzadeh, M.F., R.R.B. von Frese, H.R. Kim, T.E. Leftwich, J.W. Kim, 2007, "Spherical prism gravity effects by Gauss-Legendre quadrature integration," Geophys. J. Int., v. 169, pp. 1-11.

Asgharzadeh, M.F., R.R.B. von Frese, H.R. Kim, 2008, "Spherical prism magnetic effects by Gauss-Legendre quadrature integration," Geophys. J. Int., v. 173, 315-333.

Blakely, R.J., 1995. Potential theory in gravity and magnetic applications, Cambridge University Press.

Cooper, G., 2004. The stable downward continuation of potential field data. Exploration Geophysics. 35, 260-265.

Dampney, C.N.G., 1969. The equivalent source technique. Geophysics. (45), 39-53.

De Santis A., Battelli, O., Kerridge, D.J., 1990. Spherical cap harmonic analysis applied to regional field modelling for Italy. J. Geomag. Geoelectr., 42, 1019-1036.

De Santis A., Torta, J.M., 1997. Spherical cap harmonic analysis: a comment on its proper use for local gravity field representation. J. Geodesy, 71, 526-532.

Fedi M., Florio G., 2002. A stable downward continuation by using the ISVD method. Geophysical J. Int., 151, 146-156.

Foster, M.R., Guinzy, N.J., 1967, The coefficient of coherence: its estimation and use in geophysical prospecting, Geophysics, 32, 602-616.

Gaya-Piqué, L.R., D. Ravat, A. de Santis, J.M. Torta, 2006. New model alternatives for improving the representation of the core magnetic field of Antarctica. Antarctic Sci. 18, 101-109.

Golynsky A., Chiappini, M. Damaske, D., Ferraccioli, F., Ferris, J., Finn, C., Ghidella, M., Isihara, T., Johnson, A., Kim, H.R., Kovacs, L., LaBrecque, J., Masolov, V., Nogi, Y., Purucker, M., Taylor, P., Torta, M., 2001. ADMAP - Magnetic Anomaly Map of the Antarctic, 1:10,000,000 scale map, in Morris P, and R von Frese, eds., BAS (Misc.) 10, Cambridge, British Antarctic Survey.

Grauch, V.J.S., 1993. Limitations on digital filtering of the DNAG magnetic data set for the conterminous US. Geophysics, 8, 1281-1296.

Hains, G.V., 1985. Spherical Cap Harmonic Analysis. J. Geophys. Res., 90(B3), 2583-2591.

472 Hains, G.V., Newitt, L.R., 1986. Canadian geomagnetic reference field. J. Geomag. Geoelectr.,
473 38, 895-921.
474 Hildenbrand, T.G., Blakely, R.J., Hinze, W.J., Keller, R., Langel, R.A., Nabighian, M., Roest
475 W.R., 1996. Aeromagnetic survey over US to advance geomagnetic research. EOS Trans.
476 Amer. Geophys. Un., 77, 265-268.
477 Hwang, C, Chen, S.K., 2007. Fully normalized spherical cap harmonics: application to the
478 analysis of sea-level data from TOPEX/POSEIDON and ERS-1. Geophysical. J. Int., 129,
479 450-460.
480 IAGA (International Association of Geomagnetism and Aeronomy), Division V, Working Group
481 V, 2005. The 10th generation international geomagnetic reference field. Geophys. J. Int., 161,
482 561–565.
483 Kim, H.R., von Frese, R.R.B., Golynsky, A.V., Taylor, P.T., Kim, J.W., 2004. Application of
484 satellite magnetic observations for estimating near-surface magnetic anomalies. Earth,
485 Planets, Space, 56, 955-966.
486 Kim, H.R., R.R.B. von Frese, Golynsky, A.V., P.T. Taylor, J.W. Kim, 2005, "Crustal
487 magnetization of Maud Rise in Antarctic and Southwest Indian Oceans, Earth, Planets, and
488 Space, v. 57, pp. 717-726.
489 Kim, H.R., Hwang, J.S., Suh, M.C., Kim, J.W., 2010. New approach in magnetic potential field
490 continuation by FFT. J. Econ. Environ. Geol. 43 (3), 249-258.
491 Kim, J.W., Hwang, J.S., von Frese, R.R.B., Kim, H.R., Lee, S.H., 2007. Geomagnetic field
492 modeling from satellite attitude control magnetometer measurements. J. Geophys. Res., 112,
493 B05105, doi:10.1029 /2005JB004042.
494 Kotzé, P.B., 2001. Spherical cap modelling of Ørsted magnetic field vectors over southern
495 Africa. Earth, Planets, Space, 53, 357-361.
496 Ku C.C., 1977. A direct computation of gravity and magnetic anomalies caused by 2- and 3-
497 dimensional bodies of arbitrary shape and arbitrary magnetic polarization by equivalent-point
498 method and a simplified cubic spline. Geophysics, 42, 610–622.
499 Kuhn, M., Featherstone, W.E., 2005. Construction of a synthetic Earth gravity model by forward
500 gravity modelling. In: Sanso F (ed) A Window on the Future of Geodesy. Springer, Berlin
501 Heidelberg New York, 350-355.

502 Lemoine et al., 1998. The Development of the Joint NASA GSFC and the National Imagery and
503 Mapping Agency (NIMA) Geopotential Model EGM96. NASA/TP-1998-206861.
504 Maus, S., Rother, M. Holme, R., Luehr, M., Olsen, N., Haak, V., 2002. First scalar magnetic
505 anomaly map from CHAMP satellite data indicates weak lithospheric field. Geophys. Res.
506 Lett., 29, 10.1029/2001GL013685.
507 Maus S., Rother, M., 2005. http://geomag.colorado.edu /litmod4.html.
508 Maus, S., U. Barckhausen, N. Bournas, J. Brozena, V. Childers, F. Dostaler, J.D. Fairhead, C.
509 Finn, R.R.B. von Frese, C. Gaina, S. Golynsky, R. Kucks, H. Lühr, P. Milligan, S. Mogren,
510 R.D. Müller, O. Olesen, M. Pilkington, R. Saltus, B. Schreckenberger, E. Thébault, F.
511 Caratori Tontini, 2009. "EMAG2: A 2-arc min resolution Earth Magnetic Anomaly Grid
512 compiled from satellite, airborne, and marine magnetic measurements," Geochemistry,
513 Geophysics, Geosystems, Q08005, v. 10, doi: 10.1029/2009GC002471, ISSN: 1525-2027.
514 Mayhew, M.A., 1982. An equivalent layer magnetization model for the United States derived
515 from satellite magnetic anomalies. J. Geophys. Res., 87, 4837-4845.
516 NOAA, 2005, http://www.ngdc.noaa.gov/geomag/WMM/.
517 Pawlowski, R.S., 1995. Preferential continuation for potential-field anomaly enhancement.
518 Geophysics, 60, 390-398.
519 Ravat, D., Whaler, K.A., Pilkington, M., Sabaka, T., Purucker, M., 2002. Compatibility of high-
520 altitude aeromagnetic and satellite-altitude magnetic anomalies over Canada. Geophysics,
521 67(2), 546-554.
522 Sabaka, T. J., N. Olsen, M. Purucker, 2004, Extending comprehensive models of the Earth's
523 magnetic field with Ørsted and CHAMP data, Geophys. J. Int., 159, 521–547.
524 Schnetzler, C.C., 1985. An estimation of continental crust magnetization and susceptibility from
525 Magsat data for the conterminous United States. J. Geophys. Res., 90, 2617-2620.
526 Strang van Hees, G., 1990. Stokes formula using Fast Fourier Techniques. Manu. Geod., 15, 235-
527 239.
528 Stroud, A. H., Secrest, D. 1966. Gaussian Quadrature Formulas. Prentice-Hall.
529 Thébault, E., Schott, J.J., Mandea, M., 2006. Revised spherical cap harmonic analysis: validation
530 and properties. J. Geophys. Res., 111, B01102, doi:10.1029/2005JB001269.
531 Thébault E., Gaya-Piqué L., 2008. Applied comparisons between SCHA and R-SCHA regional
532 modeling techniques. Geochem. Geophys. Geosys, 9, doi:10.1029/2008GC001953.

Verhoef, J., Roest, W.R., Macnab, R., Arkani-Hamed, J., Members of the Project Team, 1996. Magnetic anomalies of the Arctic and North Atlantic Oceans and adjacent land areas; GSC Open File 3125, Parts a and b (CD_ROM and project report); Geological Survey of Canada, Dartmouth, NS.

von Frese R.R.B., Hinze, W.J., Braile, L.W., 1981. Spherical earth gravity and magnetic anomaly analysis by equivalent point source inversion. Earth Planet. Sci. Lett. 53, 69-83.

von Frese, R.R.B, Ravat, D.N., Hinze, W.J., McGue, C.A., 1988. Improved inversion of geopotential field anomalies for lithospheric investigations, Geophysics., 53, 375-385.

von Frese, R.R.B, Kim, H.R., Tan, L., Kim, J.W., Taylor, P.T., Purucker, M.E., Alsdorf, D.E., Raymond, C.A., 1999. Satellite magnetic anomalies of the Antarctic crust. Annali di Geofisica, 42, 309-326.

von Frese, R.R.B., H.R. Kim, 2003. "Satellite magnetic anomalies for lithospheric exploration," in: P. Stauning, H. Lühr, P. Ultré-Guérard, J. LaBrecque, M. Purucker, F. Primdahl, J.L. Jørgensen, F. Christiansen, P. Høeg, and K.B. Lauritsen (Ed.s), ØIST-4 Proceedings (4th Ørsted International Science Team Conference), 115-118, Narayana Press, Copenhagen.

von Frese, R.R.B., Kim, H.R., Taylor, P.T., Asgharzadeh, M.F., 2005. Reliability of Champ anomaly continuation. in: C. Reigber, H. Lühr, P. Schwintzer, J. Wickert (Eds.), Earth Observation with CHAMP Results from Three Years in Orbit, Springer Verlag, Heidelberg, 287-292.

von Frese, R.R.B., A.V. Golynsky, H.R. Kim, L. Gaya-Piqué, E. Thébault, M. Chiappini, M. Ghidella, A. Grunow, and the ADMAP Working Group, 2008, "The next generation Antarctic digital magnetic anomaly map," in: Cooper, A.K., and C.R. Raymond (Eds.), Proceedings of the 10th ISAES, USGS Open-File Rept. 2007-1047, doi: 10.3133/of2007.srp163.

LIST OF TABLES

Table 1. Performance statistics for using minimum curvature (MC) and Magsat (**Figure 3(B)**), Ørsted (**Figure 3(D)**), and CHAMP (**Figure 3(F)**) magnetic anomalies to fill a simulated gap in aeromagnetic anomaly coverage. The prediction statistics include the root-mean-square (RMS) difference, the correlation coefficient (CC), and related noise (N) levels. In the right four columns, the upper triangular portion gives the relative noise reductions for the gap predictions from the various constraints.

Table 2. Statistics of synthetic gravity data at 20, 10, and 0 km and correlation coefficients shown in **Figure 9** (unit: mGal).

Table 3. Statistics and correlation coefficients of radial component of KOMPSAT-1 measurements estimated at satellite (685 km), U2 (20 km), and Earth surface (0 km) as shown in **Figure10** (unit: nT).

LIST OF FIGURES

Figure 1. Normalized amplitude spectra from geomagnetic surveys at typical satellite (400 km), U2 (20km), and airborne (1 km) altitudes (adapted from Hildenbrand et al., 1996).

Figure 2. Location of the 5 crustal prisms. All prisms were 25 km thick with tops at 5 km below sea level and located in Balkan region between 34^{o} - 43^{o} N and 21^{o}- 30^{o} W.

Figure 3. Gravity effects (mGal) from five prisms in the spherical coordinates modeled (A) directly from the GLQ integration, (B) by joint EPS inversion of the 10 km and 400 km fields, (C) by single EPS inversion with the 10 km field, and (D) by single EPS inversion with 400 km field.

Figure 4. Magnetic effects (nT) from five prisms in the spherical coordinates modeled (A) directly from the GLQ integration, (B) by joint EPS inversion of the 10-km and 400-km

588 fields, (C) by single EPS inversion with the 10-km field, and (D) by single EPS inversion
589 with 400-km field.
590
591 **Figure 5**. Comparison between the modeled and estimated (A) gravity (mGal) and (B) magnetic
592 fields (nT) in **Figure 3** and **Figure 4**, respectively: (upper) correlation coefficient,
593 (middle) root-mean-square (RMS) difference, and (lower) Log (RMS).
594
595 **Figure 6.** Estimating near-surface magnetic effects to fill in regional gaps in the ADMAP
596 airborne and marine anomaly survey coverage (Kim et al., 2004). (A) ADMAP near-
597 surface magnetic anomalies for the West Antarctic Peninsula and surrounding marine
598 areas at 5 km altitude. (B) **Map A** low-pass filtered for 400-km and longer wavelengths
599 with simulated gap outlined in white. (C) Simulated Magsat anomalies at 400 km altitude
600 from a crustal prism model of **Map B** evaluated to 3-nT accuracy. (D) Near-surface
601 magnetic anomaly estimates at 5 km altitude with the coverage gap filled in using the
602 simulated Magsat in **Map C**. (E) Simulated CHAMP anomalies at 350 km altitude
603 evaluated at 0.3-nT accuracy. (F) Near-surface magnetic anomaly estimates at 5 km
604 altitude with the coverage gap filled in using the simulated CHAMP data in **Map E**. (G)
605 Simulated Ørsted anomalies at 700 km altitude evaluated at 0.3-nT accuracy. (H) Near-
606 surface magnetic anomaly estimates with the coverage gap filled in using the simulated
607 Ørsted data in **Map G**.
608
609 **Figure 7**. Comparisons of magnetic anomaly gap predictions with a recently surveyed portion of
610 the regional gap located east of Coats Land and the Shackleton Range in Antarctica (Kim
611 et al., 2007). (A) Recently surveyed aeromagnetic anomalies within the red-bordered
612 rectangular area and (B) their 200-km and longer low-pass filtered components compare
613 well with (C) the gap predictions over the survey area obtained using joint CHAMP and
614 Ørsted data and the earlier aeromagnetic anomalies. The gap predictions from (D)
615 minimum curvature and (E) the spherical harmonic geomagnetic field model MF4 (Maus
616 and Rother, 2005) are also shown. The correlation coefficients between the regional
617 survey components in Map B and the predictions in **Map C**, **Map D**, and **Map E** are
618 0.45, -0.5, and -0.18, respectively.

Figure 8. Gravity anomalies calculated at 0 km (A), 16 km (B), and 20 km (C) from prism models. **Map B** gives the differentially continued anomalies at 16 km from the multi-altitude FT using the anomalies from **Map A** and **Map C**. **Map B** gives the related anomaly differences (B - D) with the (minimum, maximum), mean, and standard deviation values listed along the bottom. **Map F** and **Map G** were calculated by conventional single-surface Fourier transform as the downward continuation of **Map C** and upward continuation of **Map A**, respectively. Their anomaly differences relative to the modeled effects at 16 km in **Map B** are given in **Maps H** and **Map I**, respectively.

Figure 9. (A) Aeromagnetic anomalies reduced-to-pole for Southern Greenland and surrounding marine areas at 20 km altitude (Verhoef et al., 1996) and conventionally upward continued to (B) 50 km, (C) 250 km, (D) 300 km, and (E) 350 km. (F) CHAMP based MF6 model estimates at 350 km (Kim et al., 2010) that were combined with the anomaly data in **Map A** for the dual-surface FT continuations at (G) 300 km, (H) 250 km, and (I) 50 km. Selected correlation coefficients between the maps are CC(E,F) = 0.16, CC(D,G) = 0.61, CC(C,H) = 0.88, and CC(B,I) = 0.99.

Figure 10. Spherical cap harmonic analysis (SCHA) model of joint gravity anomalies at 20 km (a) and 0 km (c) altitudes evaluated at the intermediate altitude of 10 km (b).

Figure 11. Spherical cap harmonic analysis (SCHA) model of radial geomagnetic field components evaluated from global KOMPSAT-1 three-axis magnetometer measurements during December 1999 at 685 km altitude (a) and SCHA model estimates at the 20 km altitude of a U2 reconnaissance survey (b) and at the Earth surface (d) (adapted from Kim et al., 2007).

Table 1. Performance statistics for using minimum curvature (MC) and Magsat (**Figure 3(B)**), Ørsted (**Figure 3(D)**), and CHAMP (**Figure 3(F)**) magnetic anomalies to fill a simulated gap in aeromagnetic anomaly coverage. The prediction statistics include the root-mean-square (RMS) difference, the correlation coefficient (CC), and related noise (N) levels. In the right four columns, the upper triangular portion gives the relative noise reductions for the gap predictions from the various constraints.

Constraint	RMS	CC	N	MC	Magsat	Ørsted	CHAMP
MC	108.7 nT	0.34	72%	0	44%	83%	94%
Magsat	98.5 nT	0.51	40%		0	70%	90%
Ørsted	74.5 nT	0.81	12%			0	67%
CHAMP	32.1 nT	0.93	4%				0

Table 2. Statistics of synthetic gravity data at 20, 10, and 0 km and correlation coefficients shown in **Figure 9** (unit: mGal).

	Min	Max	Standard Deviation	Correlation Coefficient		
				at 20 km	at 10 km	at 0 km
at 20 km	- 284.87	250.47	65.01	-	0.998	0.991
at 10 km	- 335.83	280.13	69.60	0.998	-	0.997
at 0 km	- 409.66	319.27	75.27	0.991	0.997	-

Table 3. Statistics and correlation coefficients of radial component of KOMPSAT-1 measurements estimated at satellite (685 km), U2 (20 km), and Earth surface (0 km) as shown in **Figure10** (unit: nT).

	Min	Max	Standard Deviation	Correlation Coefficient		
				at 685 km	at 20 km	at 0 km
at 685 km	- 55378.50	- 13201.80	8821.38	-	0.991	0.990
at 20 km	- 70959.30	- 22931.40	10743.58	0.991	-	1.0
at 0 km	- 71515.10	- 23270.30	10813.16	0.990	1.0	-

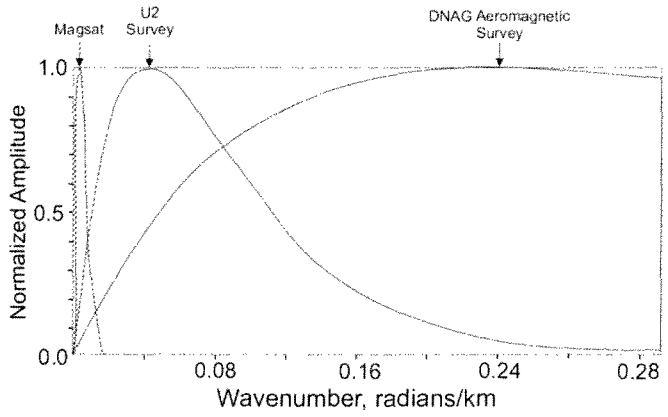

Figure 1. Normalized amplitude spectra from geomagnetic surveys at typical satellite (400 km), U2 (20km), and airborne (1 km) altitudes (adapted from Hildenbrand et al., 1996).

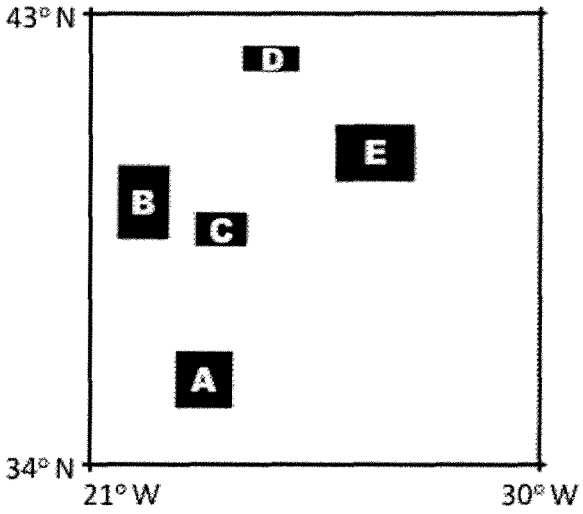

Figure 2. Location of the 5 crustal prisms. All prisms were 25 km thick with tops at 5 km below sea level and located in Balkan region between 34° - 43° N and 21°- 30° W.

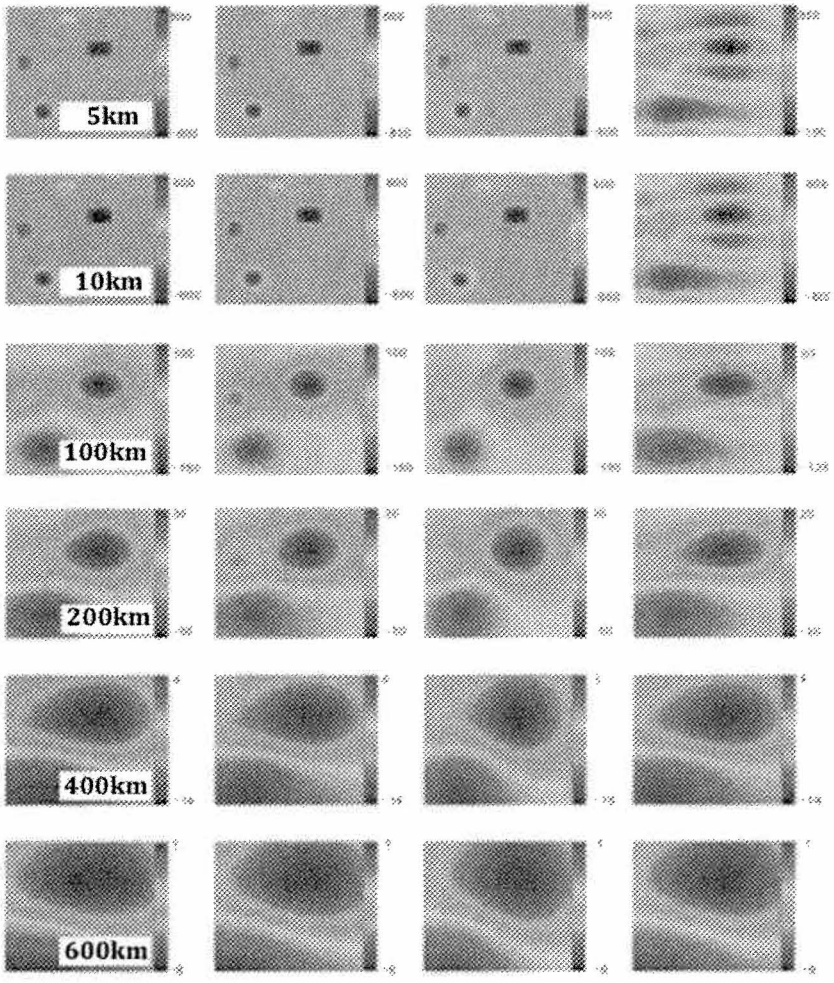

Figure 3. Gravity effects (mGal) from five prisms in the spherical coordinates modeled (A) directly from the GLQ integration, (B) by joint EPS inversion of the 10 km and 400 km fields, (C) by single EPS inversion with the 10 km field, and (D) by single EPS inversion with 400 km field.

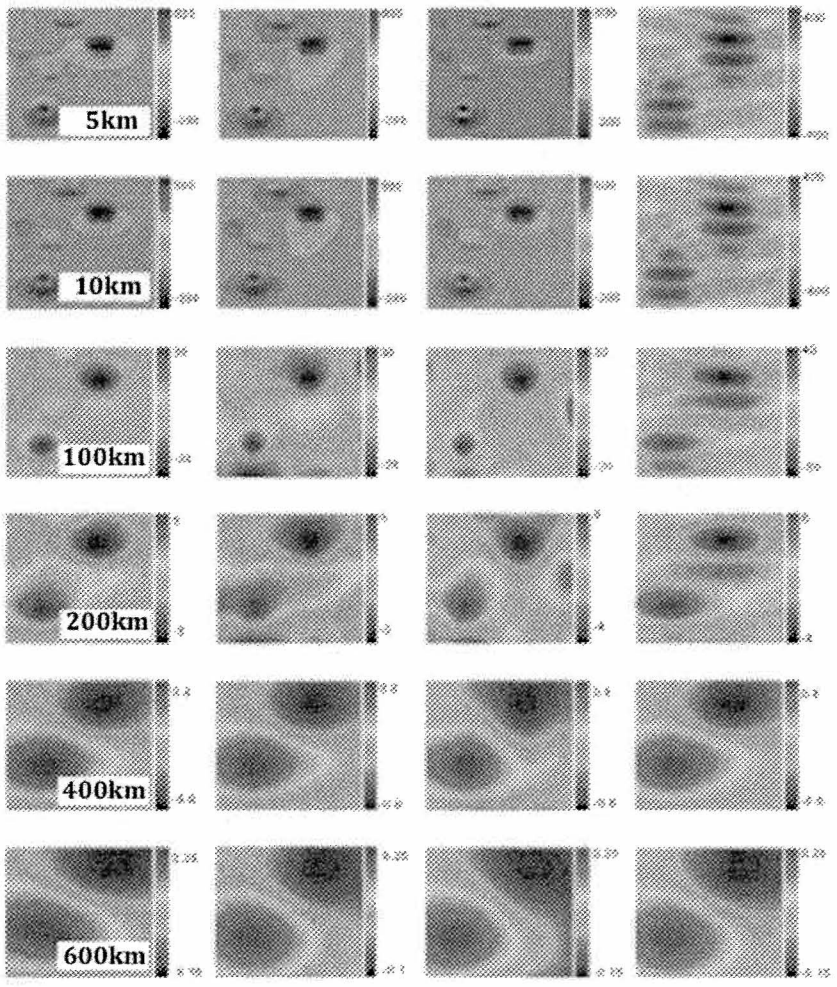

Figure 4. Magnetic effects (nT) from five prisms in the spherical coordinates modeled (A) directly from the GLQ integration, (B) by joint EPS inversion of the 10-km and 400-km fields, (C) by single EPS inversion with the 10-km field, and (D) by single EPS inversion with 400-km field.

A) Gravity Anomalies (B) Magnetic Anomalies

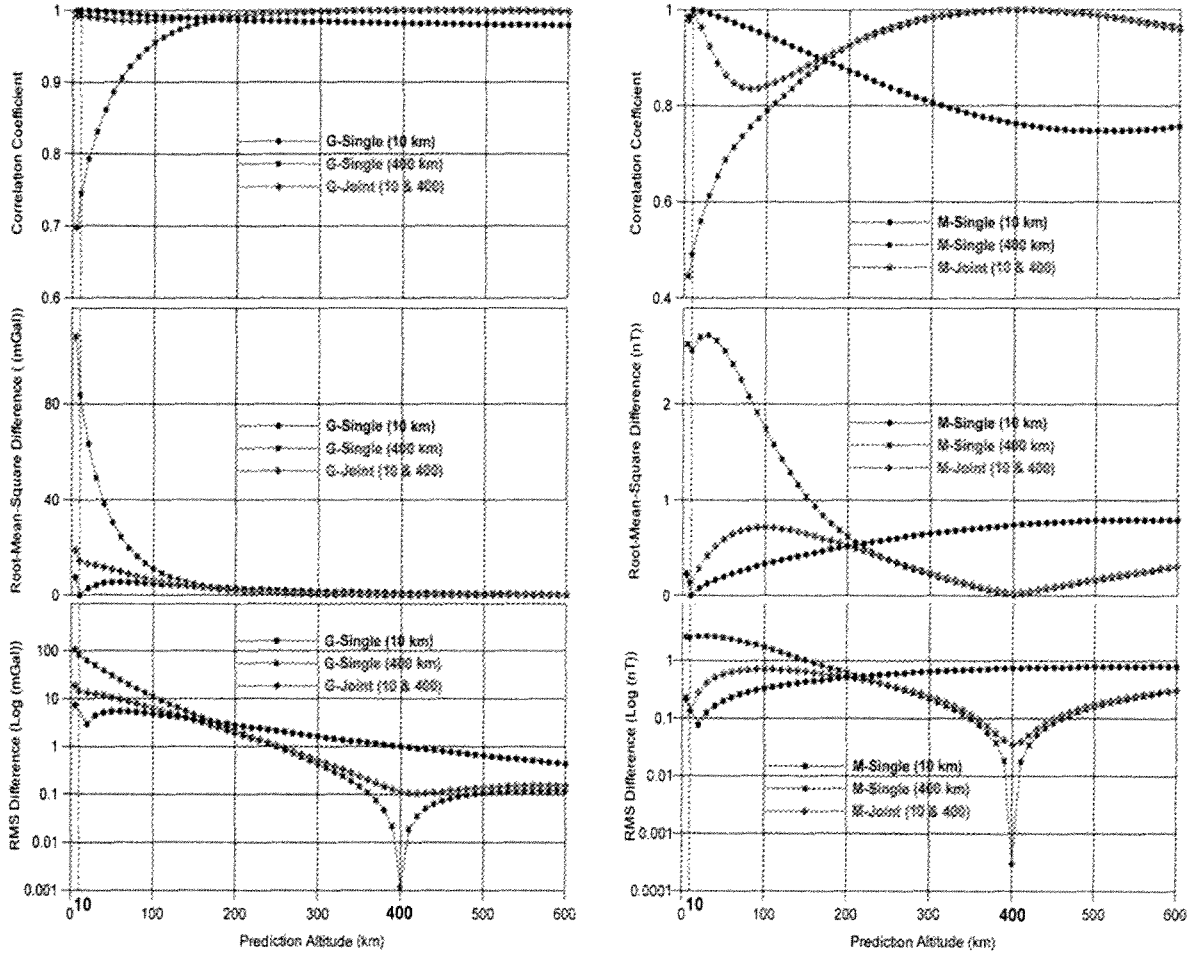

Figure 5. Comparison between the modeled and estimated (A) gravity (mGal) and (B) magnetic fields (nT) in **Figure 3** and **Figure 4**, respectively: (upper) correlation coefficient, (middle) root-mean-square (RMS) difference, and (lower) Log (RMS).

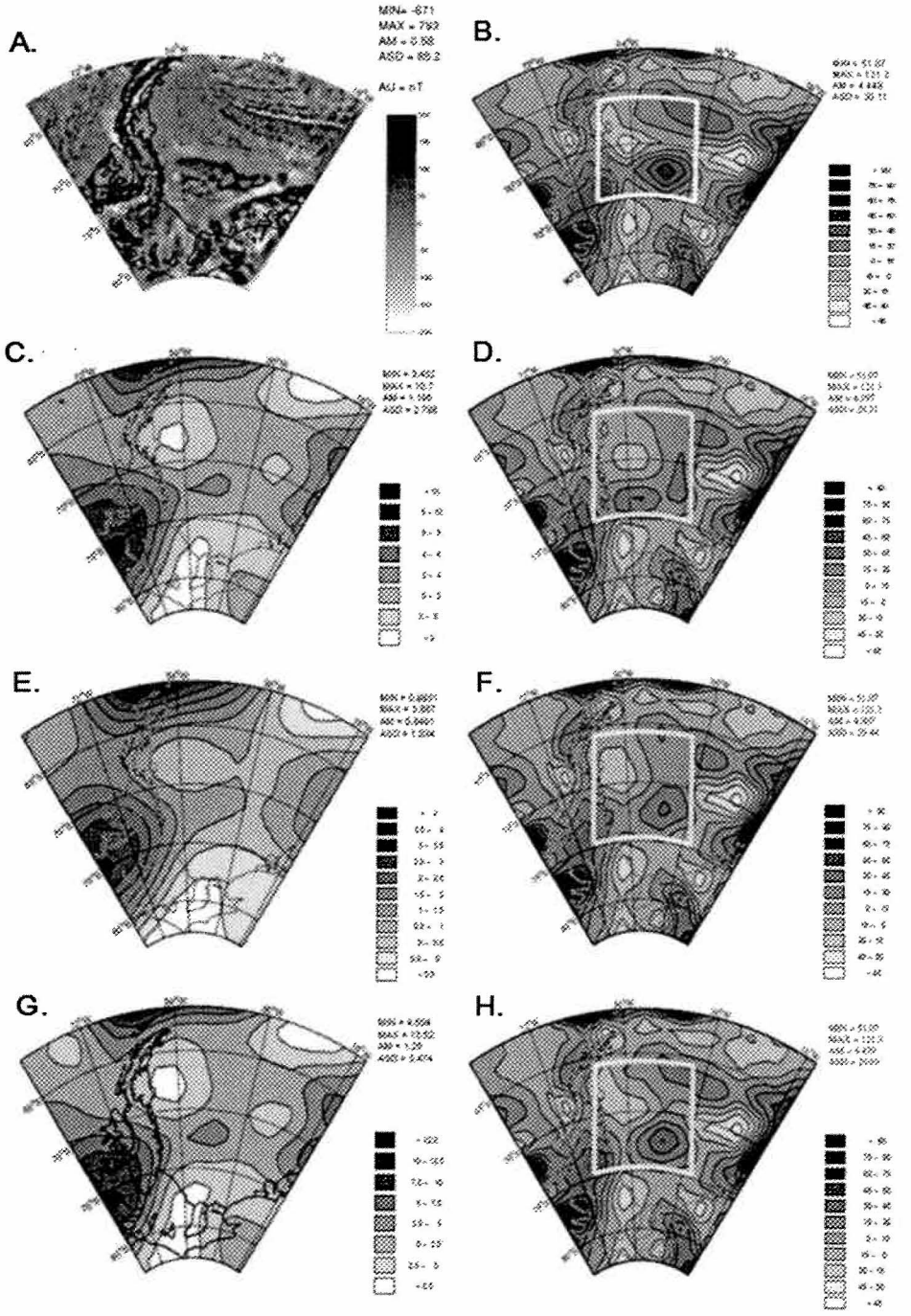

Figure 6. Estimating near-surface magnetic effects to fill in regional gaps in the ADMAP airborne and marine anomaly survey coverage (Kim et al., 2004). (A) ADMAP near-surface magnetic anomalies for

the West Antarctic Peninsula and surrounding marine areas at 5 km altitude. (B) **Map A** low-pass filtered for 400-km and longer wavelengths with simulated gap outlined in white. (C) Simulated Magsat anomalies at 400 km altitude from a crustal prism model of **Map B** evaluated to 3-nT accuracy. (D) Near-surface magnetic anomaly estimates at 5 km altitude with the coverage gap filled in using the simulated Magsat in **Map C**. (E) Simulated CHAMP anomalies at 350 km altitude evaluated at 0.3-nT accuracy. (F) Near-surface magnetic anomaly estimates at 5 km altitude with the coverage gap filled in using the simulated CHAMP data in **Map E**. (G) Simulated Ørsted anomalies at 700 km altitude evaluated at 0.3-nT accuracy. (H) Near-surface magnetic anomaly estimates with the coverage gap filled in using the simulated Ørsted data in **Map G**.

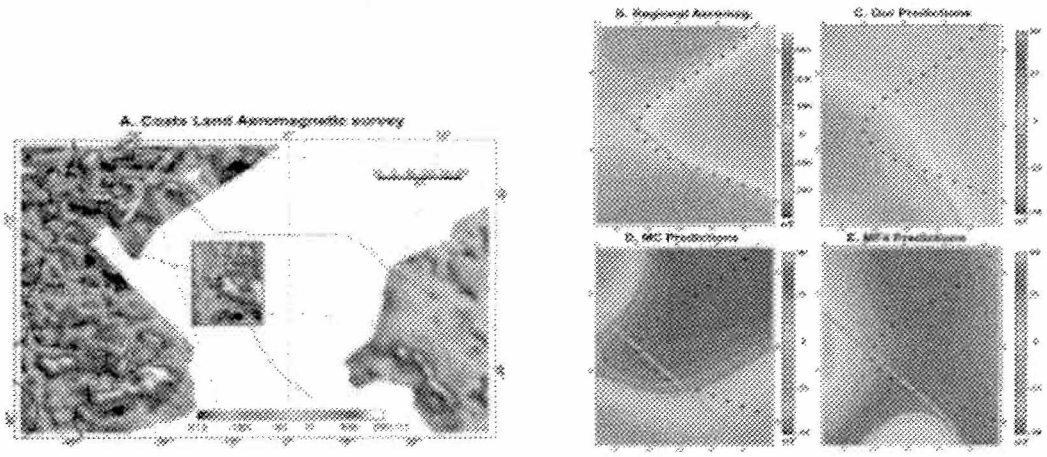

Figure 7. Comparisons of magnetic anomaly gap predictions with a recently surveyed portion of the regional gap located east of Coats Land and the Shackleton Range in Antarctica (Kim et al., 2007). (A) Recently surveyed aeromagnetic anomalies within the red-bordered rectangular area and (B) their 200-km and longer low-pass filtered components compare well with (C) the gap predictions over the survey area obtained using joint CHAMP and Ørsted data and the earlier aeromagnetic anomalies. The gap predictions from (D) minimum curvature and (E) the spherical harmonic geomagnetic field model MF4 (Maus and Rother, 2005) are also shown. The correlation coefficients between the regional survey components in Map B and the predictions in **Map C**, **Map D**, and **Map E** are 0.45, -0.5, and -0.18, respectively.

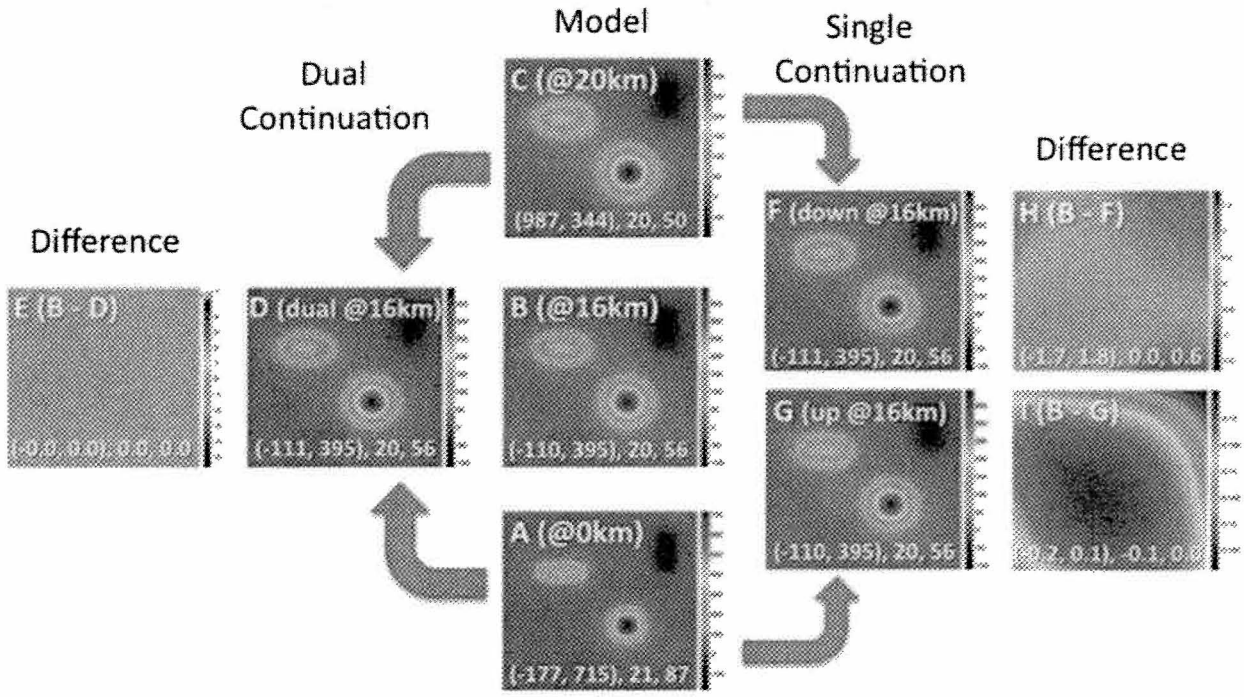

Figure 8. Gravity anomalies calculated at 0 km (A), 16 km (B), and 20 km (C) from prism models. **Map B** gives the differentially continued anomalies at 16 km from the multi-altitude FT using the anomalies from **Map A** and **Map C**. **Map B** gives the related anomaly differences (B - D) with the (minimum, maximum), mean, and standard deviation values listed along the bottom. **Map F** and **Map G** were calculated by conventional single-surface Fourier transform as the downward continuation of **Map C** and upward continuation of **Map A**, respectively. Their anomaly differences relative to the modeled effects at 16 km in **Map B** are given in **Maps H** and **Map I**, respectively.

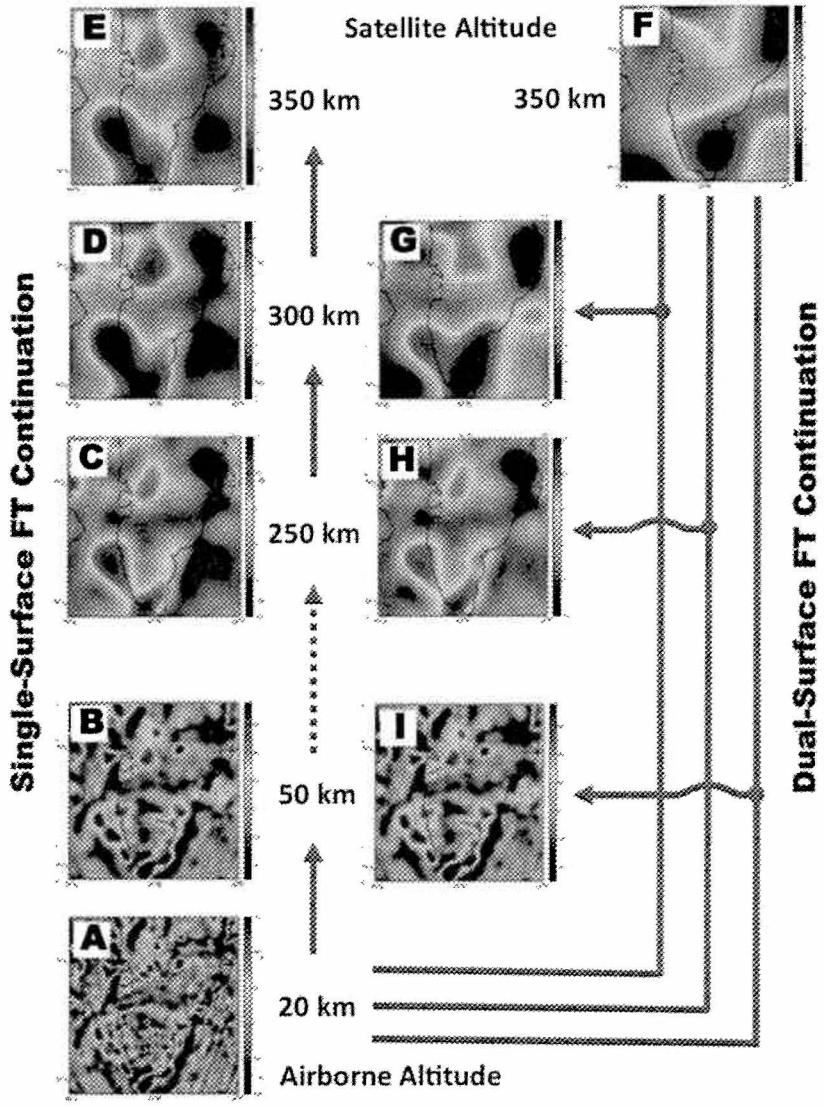

Figure 9. (A) Aeromagnetic anomalies reduced-to-pole for Southern Greenland and surrounding marine areas at 20 km altitude (Verhoef et al., 1996) and conventionally upward continued to (B) 50 km, (C) 250 km, (D) 300 km, and (E) 350 km. (F) CHAMP based MF6 model estimates at 350 km (Kim et al., 2010) that were combined with the anomaly data in **Map A** for the dual-surface FT continuations at (G) 300 km, (H) 250 km, and (I) 50 km. Selected correlation coefficients between the maps are CC(E,F) = 0.16, CC(D,G) = 0.61, CC(C,H) = 0.88, and CC(B,I) = 0.99.

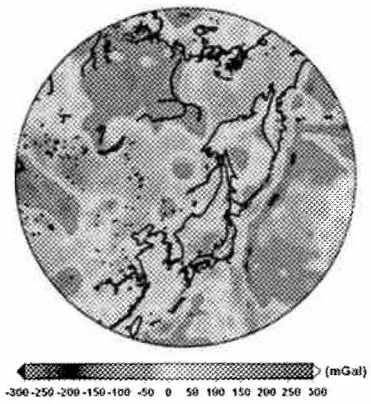

(a) 20 Km

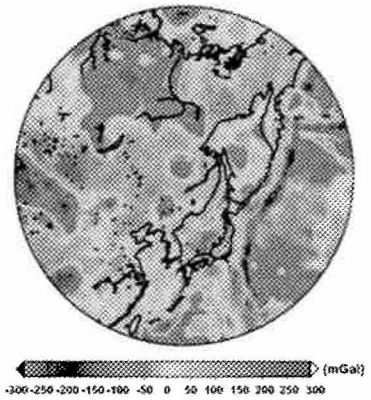

(b) 10 km

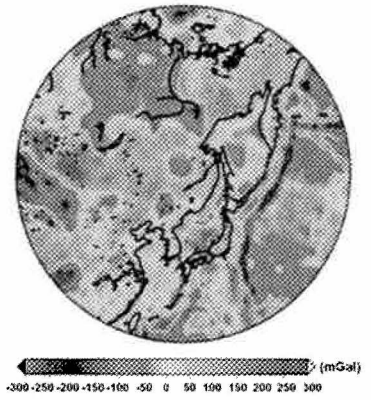

(c) 0 km

Figure 10. Spherical cap harmonic analysis (SCHA) model of joint gravity anomalies at 20 km (a) and 0 km (c) altitudes evaluated at the intermediate altitude of 10 km (b).

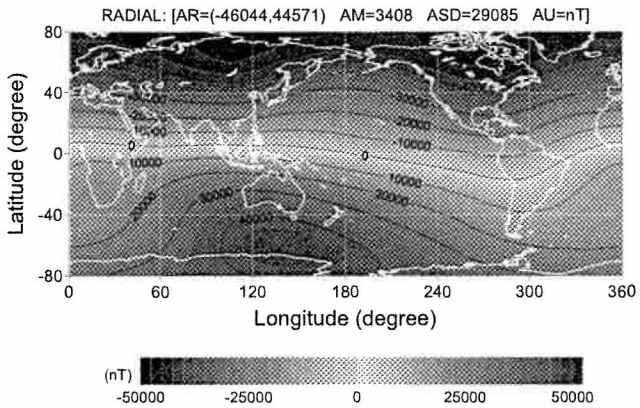

(a) Global KOMPSAT-1 (685 Km)

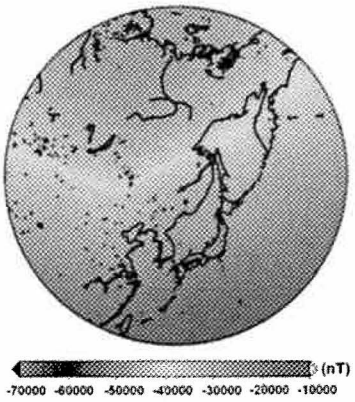

(b) Satellite (685 Km)

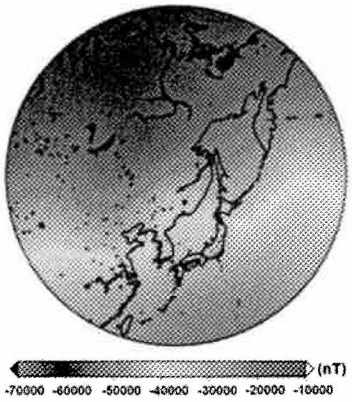

(c) U2 (20 Km)

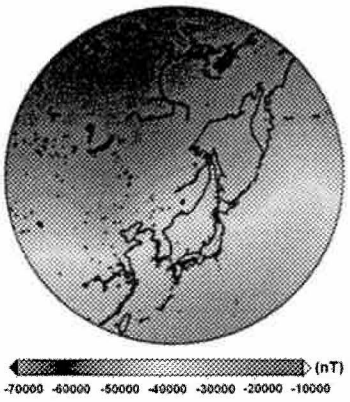

(d) Earth Surface (0 Km)

Figure 11. Spherical cap harmonic analysis (SCHA) model of radial geomagnetic field components evaluated from global KOMPSAT-1 three-axis magnetometer measurements

during December 1999 at 685 km altitude (a) and SCHA model estimates at the 20 km altitude of a U2 reconnaissance survey (b) and at the Earth surface (d) (adapted from Kim et al., 2007).